Journal of Materials Chemistry A

ROYAL SOCIETY OF CHEMISTRY

PAPER

View Article Online
View Journal | View Issue

Cite this: J. Mater. Chem. A, 2026, 14, 1123

Gas evolution in Ruddlesden–Popper-type intercalation cathodes in all-solid-state fluoride-ion-batteries: implications on battery performance and synthesis of highly oxidized oxyfluorides

Tommi Hendrik Aalto, [a] Jonas Jacobs, [b] Felix Frey,[a] Dörthe Schiewe[c] and Oliver Clemens *[a]

In this work, we report the gas evolution behavior of two common intercalation-based cathode materials for fluoride-ion-batteries (La_2NiO_4 and La_2CoO_4) by chemical fluorination and electrochemical fluorination, as well as the thermal stability of the electrochemically fluorinated active materials. Variable-temperature X-ray diffraction with coupled mass spectrometry shows that the fluorinated phases of both active materials release oxygen after oxidative fluorination using AgF. Differential electrochemical mass spectrometry revealed that significant CO_2, CO and NO evolution takes place during electrochemical fluorination, but O_2 evolution could not be detected. Consequently, the gas evolution observed does not compromise the long-term stability of the cell performance. Variable-temperature X-ray diffraction of the charged cathode composites reveals that the electrochemically fluorinated products decompose once heated beyond 300 °C, and then undergo similar phase evolution behavior as observed in chemical fluorination. Thus, we conclude that oxygen evolution in RP-type materials on oxidative fluorination requires thermal activation beyond the operational temperature of 170 °C, and that it can be kinetically suppressed regardless of the reduced Fermi level induced on fluorination. Our findings indicate that concepts used for the oxidative topochemical fluorination of materials need to be reconsidered: the choice of fluorination conditions must be carefully adopted to the changes of electronic structure induced and the temperature dependence of the oxygen evolution of the highly oxidized state.

Received 29th August 2025
Accepted 14th November 2025

DOI: 10.1039/d5ta07033c

rsc.li/materials-a

1 Introduction

While lithium-ion-batteries (LIBs) owe their commercial success at least partly to their high voltage, cathode materials used within high voltage LIBs show side reactions on charging, where instead of the transition metal being oxidized further, the oxide ions get oxidized. This can take place either in the form of lattice oxygen redox (LOR) which is considered reversible since the oxidized oxygen species still reside in the crystal structure,[1–7] or in the form of oxygen release which is irreversible since the gaseous products leave the solid.[8–15]

Anion redox has recently been reported to be a major contributor to reversible capacity in all-solid-state fluoride-ion-batteries (ASS-FIBs).[16–19] Wang *et al.* first reported reversible lattice oxygen redox for ASS-FIBS for the $n = 2$ Ruddlesden–Popper (RP) material $Sr_3Fe_2O_5F_2$ by soft X-ray absorption spectroscopy.[17] More recent publications showed that anion redox chemistry can be enabled for other transition-metal containing RP-oxides[18] or perovskites,[20] as well as sulfur redox in oxysulfides[19] and nitrogen redox in Cu_3N[16] demonstrating the formation of oxygen and nitrogen molecules using resonant inelastic X-ray scattering. While oxygen or nitrogen release was briefly mentioned in these studies, no further investigations were undertaken.

Zhang *et al.* reported oxide–fluoride exchange in the chemical fluorination of $La_3Ni_2O_7$ using CuF_2 forming a $La_3Ni_2O_{5.5}F_{3.5}$ fluorinated phase, though the oxygen release was not measured directly.[21] A combination of thermogravimetric analysis with coupled mass spectrometry (TG-MS) was used along with phase quantification by X-ray diffraction to determine the final oxygen content of the fluorinated phase.

In this study, we investigate the gas evolution behavior of two common cathode active materials for ASS-FIBs (La_2NiO_4/La_2CoO_4) by chemical fluorination using AgF observed *via in situ* XRD with coupled mass spectrometry (XRD-MS) and differential electrochemical mass spectrometry (DEMS). The results show that chemical fluorination at 300 °C leads to

[a]University of Stuttgart, Institute for Materials Science, Department of Chemical Materials Synthesis, Heisenbergstraße 3, 70569 Stuttgart, Germany. E-mail: oliver.clemens@imw.uni-stuttgart.de; Fax: +49 711 685 51933

[b]Martin Luther University Halle-Wittenberg, Department of Chemistry, Inorganic Chemistry, Kurt-Mothes-Straße 2, 06120 Halle, Germany

[c]University of Stuttgart, Institute for Chemical Process Engineering, Böblinger Straße 78, 70199 Stuttgart, Germany

significant release of oxygen, while electrochemical fluorination at 170 °C conserves the oxygen content in the material. Heating the electrochemically fluorinated compounds to 300 °C as in chemical fluorination leads to decomposition, showing that the products are metastable and oxygen release was only inhibited kinetically. Thus, our findings show that RP-type cobaltates and nickelates could in principle maintain their lattice oxygen regardless of the low Fermi level introduced on electrochemical fluorination, and that LOR with oxygen release is inhibited at the reduced operation temperature of FIBs.

2 Experimental

2.1 Synthesis

La_2CoO_4 and La_2NiO_4 samples for chemical fluorination with AgF were synthesized from precursors obtained by a citric acid-assisted combustion method. Stochiometric amounts of La_2O_3 (ChemPUR, 99.99%; dried at 900 °C for 10 h), and Ni powder (Sigma-Aldrich, 99.99%) or $Co(NO_3)_3 \cdot 6H_2O$ (Sigma-Aldrich, 98%) were dissolved in approx. 25 mL of distilled water with the addition of a few drops of concentrated HNO_3. Citric acid (Anhydrous, Grüssing, 99%; molar ratio metal ions : citric acid = 1 : 3) was added while stirring. The resulting clear solution was subsequently dried on a hot plate at 120 °C until gel formation. The gels were further heated at 350 °C until ignition. The resulting powders were heated in air at 650 °C for 10 h to ensure complete removal of the organic matrix. La_2NiO_4 was afterwards obtained from calcinating this precursor at 1050 °C for 10 h in air. La_2CoO_4 was obtained after calcinating the precursor at 1300 °C for 12 h in an atmosphere of flowing Argon with a purity of 99.999% (150 mL min^{-1}).

Before mixing with AgF, both oxides were annealed at 300 °C for 12 h in flowing N_2, subsequently put under high vacuum conditions for 12 h before storing them in an Ar filled glove box. Oxide and AgF (Sigma-Aldrich, 99.9%) mixtures in molar ratios of oxide 1 : 2 AgF were prepared by hand-grinding stochiometric amounts in the glove box.

About 10 mg of these mixtures were filled in capillaries ($d_{ext.}$ = 0.8 mm) which were equipped with the self-made *in situ* XRD-MS adapter head (*vide infra*) and temporarily sealed with wax before retrieving them from the glove box.

For electrochemical fluorination, La_2NiO_4 was synthesized by heating a hand-ground mixture of La_2O_3 (Alfa Aesar, 99.9%, pre dried at 1200 °C for 12) and NiO (Thermo Fisher, 99%) to 1200 °C for 8 hours in air with an intermediate regrind.[22] La_2CoO_4 was synthesized by ball-milling La_2O_3 and Co_3O_4 (Thermo Fisher, 99.7%) in isopropanol for 1 h at 600 rpm and subsequently heating to 1300 °C in argon flow.[23]

$La_{0.9}Ba_{0.1}F_{2.9}$ was synthesized by ball milling LaF_3 (Strem, 99.9%) and BaF_2 (Strem, 99%) for 12 h in 50 mL ZrO_2 jars with 10 ZrO_2 balls of 10 mm diameter in argon atmosphere cathode composites of $La_{0.9}Ba_{0.1}F_{2.9}$, La_2NiO_4 or La_2CoO_4 and conductive carbon (Super P, Alfa Aesar, 99+%) were prepared by ball-milling 60 wt% $La_{0.9}Ba_{0.1}F_{2.9}$, 30 wt% active material and 10 wt% Super P for 2 h at 250 rpm in the same ball-milling jars and balls as mentioned above under argon atmosphere. A composite without active material was made by ball milling 90 wt% $La_{0.9}Ba_{0.1}F_{2.9}$ with 10 wt% Super P at the same parameters. The composites were dried at 170 °C for 15 h in vacuum after ball milling.[24]

Electrochemical cells of 7.3 mm diameter were prepared by pressing 5 mg of the cathode composite and 10 mg of PbF_2 on either side of a 200 mg layer of the $La_{0.9}Ba_{0.1}F_{2.9}$ solid electrolyte. These layers were briefly compressed at 230 MPa before a Pb foil current collector was applied to the PbF_2 anode side. The whole cell, including the current collector, was then compacted at 460 MPa for 90 s, before being extracted from the hardened-steel die set.

2.2 Coupled *in situ* XRD and mass spectrometry

For analyzing the gaseous reaction products of the chemical fluorination with AgF, an *in situ* XRD-MS setup was used. A scheme of this setup is shown in Fig. 1. This setup consists of a Swagelok cross piece fitting to which the sample capillary can be attached *via* a stainless-steel ferrule which is glued to the head of the capillary. The gas transfer capillary (heated to 120 °C) of a mass spectrometer (Pfeiffer Vacuum OmniStar GSD 350) is then inserted into the sample capillary from the opposite port in such a way that it is situated approx. 15 mm above the sample surface. The carrier gas is flowing over the opening of the capillary through the two other ports, allowing control of the gas atmosphere.

Connecting the sample capillary to the Swagelok fitting was performed under a flow of N_2 gas in order to avoid introducing O_2 and H_2O into the system. After connecting the capillary to the

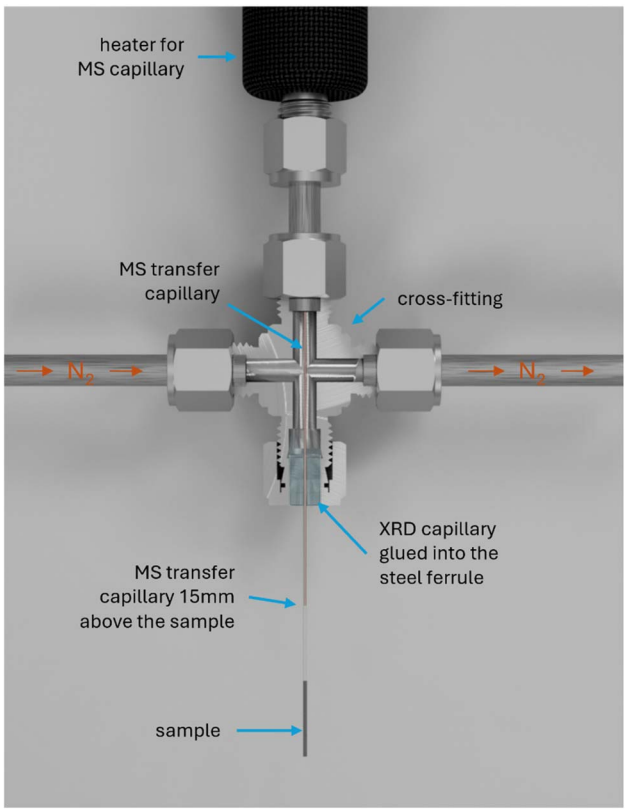

Fig. 1 Cross-section rendering of the XRD-MS capillary setup used for the analysis of gaseous reaction products.

setup, the system was subjected to three purge evac. cycles and the purge gas (N_2) was afterwards allowed to flow through the setup for 12 h before starting the experiment.

To perform the temperature dependent XRD-MS study, the capillary reactor is introduced in a HT1 capillary furnace (STOE) which is used together with a STADI MP transmission powder diffractometer (STOE). This device works with monochromatic Mo-$K_{\alpha1}$ radiation and is equipped with one MYTHEN2 1K Si-strip detector module (DECTRIS).

The following parameters were used for the *in situ* XRD experiments of this work. Diffraction patterns were recorded in the range of $2\theta = 8$–$40°$ with a datapoint increment of 0.015° for 7 min total acquisition time. The sample capillary was heated stepwise from 50 to 150 °C with steps of 10 °C and 25 °C min^{-1} and from 150 to 300 °C with steps of 5 °C and a 5 °C min^{-1} heating rate. A diffraction pattern was recorded after every step. The samples were kept at 300 °C for a further 20 h, and diffraction patterns were recorded repeatedly until the end of the experiment.

2.3 High-temperature DEMS setup

In order to measure gas evolution from ASS-FIBs, a DEMS setup was constructed which allows for heating the cell pellet up to 200 °C. To avoid outgassing, the entire setup is constructed from stainless steel, and the heated zone is well-separated from the Viton O-rings to suppress gas permeation. The O-rings were de-gassed by heating at 100 °C in vacuum for 15 h to further reduce gas permeation through the Viton polymer. For every measurement, all O-rings which seal the sample chamber were exchanged for freshly de-gassed O-rings. Without these precautions, significant quantities of nitrogen and oxygen would outgas into the cell container over the course of one hour leading to oxygen concentrations in the order of 5–10 ppm.

The stainless-steel components which will be heated during operation were heated to ~400 °C in air before use to establish a sufficient oxide layer to avoid further reaction of gases with the stainless-steel surface. The cell pellet was placed between two stainless steel current collector pins, and a spring was used to contact the pellet. One of the current collector pins was separated from the outer steel tube using a glass tube to prevent a short-circuit. A close-up rendering of the setup with the pellet in its measurement position is shown in Fig. 2.

Leybold high vacuum valves were used to allow for closing and opening the cell container to an argon flow. Since the valves used were manual operation valves, they were equipped with 3D-printed couplings and stepper motors which were operated by an Arduino Uno microcontroller to allow automatized operation. While the cell container is closed, a bypass is opened to measure the argon (99.999%) carrier gas for a background signal while the evolved gases accumulate in the cell container. In 1 h intervals, the cell container is then opened while the bypass is closed, to flush all evolved gases towards the mass spectrometer capillary. The resulting concentration peaks from flushing the cell container reflect the gas evolution in the time between flushing cycles. They were integrated over a locally determined baseline for every concentration peak using a python script to obtain the gas evolution values.

The mass spectrometer used for the measurements in this study was a Balzers Prisma QMS200. The gases from the capillary entered a pre-evacuation chamber with a pressure of ~25 mbar from which they pass through a leak valve into the high vacuum chamber of the mass spectrometer which is operated at an approximate pressure in the order of 10^{-7} mbar.

The mass spectrometer was calibrated for oxygen using different calibration gases (50 ppm, 100 ppm and 1000 ppm O_2 in N_2) as well as using air for calibration of CO_2 (420 ppm CO_2 in air). Since the carrier gas for the calibration was nitrogen or air, the ratio $r(O_2) = I(O_2)/I(N_2)$ or $r(CO_2) = I(CO_2)/(I(N_2) + I(O_2))$ was the calibrated quantity, resulting in a factor of 1.36 and 0.53 to convert from $r(O_2)$ to $c(O_2)$ and $r(CO_2)$ to $c(CO_2)$ respectively. For the other gases, no calibration gas was available so a semiquantitative approach was applied, where the ratio $r(\text{gas}) = I(\text{gas})/I(\text{Ar})$ was assumed to reflect its concentration directly. The concentration values of the gases which are only semiquantitative are denoted by a unit of "~ppm" instead of "ppm" for the calibrated gases. We assume a 30–50% uncertainty for the values of CO and NO, due to the values of the calibration factors for CO_2 and O_2 as given above; regardless of the uncertainty of the absolute value, the trends discussed in this article are not affected due to the linear correlation of the ion current to the concentration.

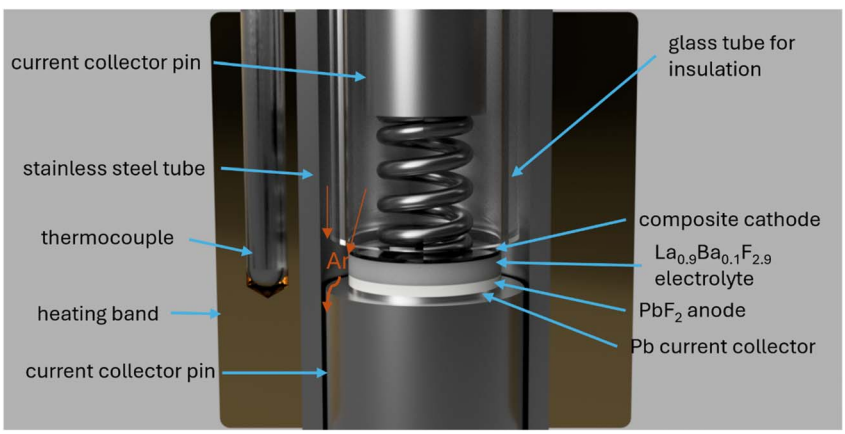

Fig. 2 Close-up cross-section rendering of the cell pellet in the DEMS setup.

2.4 Electrochemical measurements

Electrochemical measurements were conducted using a Biologic SP150 single channel potentiostat. A constant current of 10 μA was used for all DEMS measurements which were limited by a cut-off voltage of 2 V *vs.* Pb/PbF_2.

2.5 X-ray diffraction of cell pellets

X-ray diffraction of cell pellets after extraction from the DEMS setup was conducted using a RIGAKU SmartLab diffractometer using a Cu K_α X-ray tube and a HyPix-3000 detector equipped with a Ni-filter to remove the K_β radiation. Measurements were always conducted in airtight sample holders which were sealed in an argon-filled glovebox.

Variable-temperature X-ray diffraction of the cells charged in the DEMS setup were carried out on an Anton Paar DHS1100 variable temperature stage operated by an Anton Paar CCU100 temperature control system. The cells were measured in dynamic vacuum ($\sim 10^{-2}$ mbar). The pellets were measured between 160 °C and 300 °C in steps of 20 °C, then held at 300 °C for 7 h. A XRD pattern was recorded every 30 minutes. This setup had to be used due to the incompatibility of the cell pellets with capillaries used for the coupled XRD-MS measurements described in Section 2.2. All patterns were recorded scanning with a step size of 0.005° 2θ and a scan speed of 1.5° 2θ min^{-1}.

2.6 Thermogravimetric analysis with coupled mass-spectrometry

Thermogravimetric analysis was carried out on a Netzsch STA 449 with a heating rate of 10 °C min^{-1}. A nitrogen flow of 40 mL min^{-1} was used to transport the exhaust gases to be analysed by a Balzers Prisma QMS200 mass spectrometer.

3 Results and discussion

3.1 *In situ* XRD with coupled mass spectrometry

La_2CoO_4 and La_2NiO_4 were fluorinated using two molar equivalents of AgF in the XRD-MS setup as described above. The final products formed can be described by the following general reaction scheme

$$La_2MO_4 + 2AgF \rightarrow La_2MO_{4-x}F_2 + 2Ag + \frac{x}{2}O_2 \quad (1)$$

while our measurements are used in order to understand the complexity of the individual reaction steps underlying this reaction equation.

The variable-temperature X-ray diffraction (VTXRD) patterns of La_2CoO_4 and La_2NiO_4 obtained during fluorination are shown in Fig. 3a and b respectively. The weight fractions of the occurring phases as well as signals for O_2 ($m/z = 32$) and F ($m/z = 19$) are additionally shown in Fig. 3c for La_2CoO_4 and Fig. 3d for La_2NiO_4, showing that F_2 release can be neglected in comparison to the evolution and release of O_2.

Upon heating the reaction mixture to 180 °C, a signal for $m/z = 19$ can be detected by the mass spectrometer (most likely originating from dissociation of F_2 by the ionization process), which marks the onset of the decomposition of AgF and therefore the start of the reaction. The fluorination of La_2CoO_4 follows a rather straightforward scheme, with a reduction of the weight fraction of the starting La_2CoO_4 *Fmmm* phase and a parallel increase of the phase fraction of a phase similar to the previously reported[23] fluorinated phase of $La_2CoO_4F_{1.2}$ with monoclinic symmetry and strongly elongated *c*-axis (~15.2 Å *vs.* ~12.7 Å) as described by Nowroozi *et al.*[23] The pattern of this phase which will be called mono LCOF was fitted by a monoclinic structure model with $P2_1/c$ unit cell symmetry which we could derive from neutron powder diffraction analysis. These samples have the stoichiometry of $La_2CoO_3F_3$ as derived from chemical analysis and a full structure description will be published elsewhere. The formation of mono LCOF is correlated with oxygen release, as can be seen in the bottom graph in Fig. 3c. A dashed line marks the time of maximum oxygen release, which coincides with the turning point of the weight fractions of La_2CoO_4 and mono LCOF meaning that the rate of phase formation mirrors the oxygen release rate. This observation implies that the mono LCOF is oxygen deficient. Also, since the reaction with two equimolar amounts of AgF only results in the fluorination of ~70% of La_2CoO_4 and the amount of fluorine lost in the atmosphere is insignificantly small, the product is most likely fluorine rich, making its stoichiometry similar to $La_2CoO_3F_3$ as mentioned above. Upon reacting La_2CoO_4 with three equivalents of AgF, almost complete conversion to $La_2CoO_3F_3$ is observed, confirming this assumption (see Fig. S1). The reaction as well as oxygen release are mostly terminated as the maximum temperature of 300 °C is reached.

For La_2NiO_4 a more complicated phase evolution is apparent:

The first phase to appear is an orthorhombically distorted version of the starting La_2NiO_4 *I4/mmm* oxide. Nowroozi *et al.*[25] as well as Jacobs *et al.*[26] already linked a similar small orthorhombic distortion of tetragonal La_2NiO_4 to small amounts of fluoride content which is why it will be referred to as *ortho* LNOF #1. This phase reaches its maximum weight fraction after 190 minutes but does not decay completely. At the end of the reaction, ~10 wt% of *ortho* LNOF #1 are still present.

A second phase appears shortly after *ortho* LNOF #1, which is similar to previously reported[25] $La_2NiO_4F_{1.8}$ with an extended *c*-lattice parameter of $c \sim 15.2$ Å as observed in electrochemical fluorination by Nowroozi *et al.*[25] However, the most prominent signal of this phase (indexed as (113) and marked with an arrow "mono LNOF" in Fig. 3b) splits into two reflections after ~220 minutes of reaction time, indicating a change to monoclinic unit cell symmetry. Due to the similarity of lattice parameters, especially the increased *c*-lattice parameter of 15.25 Å, this phase was fitted using the structure of previously reported (ref. 27) $La_2NiO_3F_3$ wtih *C2/c* symmetry described by Wissel *et al.*[27] In the following, this phase is denoted with mono LNOF. The oxygen deficiency and fluorine content lower than three F per formula unit is implied from the observed oxygen release simultaneously to the monoclinic distortion and the absence of further non-fluorinated phases. This phase reaches the maximum weight fraction ~240 minutes of reaction time and decays completely until the end of the experiment.

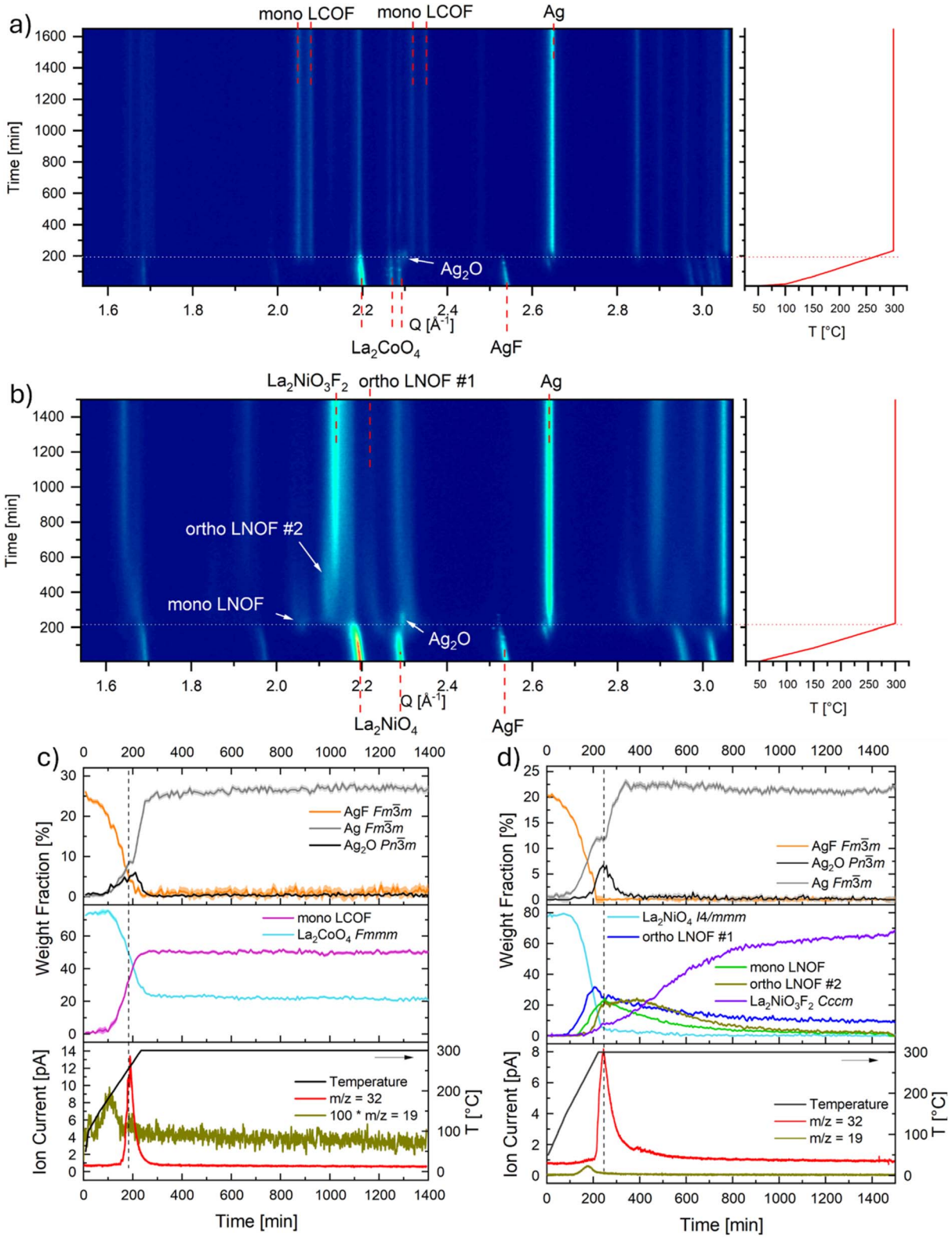

Fig. 3 Heatmap-plot of the VTXRD patterns of (a) La_2NiO_4 and (b) La_2CoO_4 obtained during fluorination using AgF. The dotted white/red line marks the time and temperature where the starting compound disappeared. Weight fractions obtained by Rietveld refinement of AgF, Ag_2O, Ag; La_2CoO_4 *Fmmm* and mono LCOF; La_2NiO_4 *I4/mmm*, *ortho* LNOF #1, mono LNOF, *ortho* LNOF #2 and $La_2NiO_3F_2$ *Cccm* as well as the ion current for $m/z = 32$ and $m/z = 19$ along with the temperature in the *in situ* XRD-MS fluorination of (c) La_2CoO_4 and (d) La_2NiO_4 using AgF. The dashed grey line marks the time of maximum oxygen release.

Signals of a third phase appear at about 200 minutes into the reaction; this phase disappears again under formation of $La_2NiO_3F_2$ as described by Wissel *et al.*[22] Thus, we assume that this phase likely has a composition between $La_2NiO_3F_2$ and that of mono LNOF, in agreement with the structural behaviour observed (decrease of *c*-axis, strong distortion of the *a*/*b*-plane). It was fitted using the structure of the phase "orthorhombic #3" from ref. 27 and will be referred to as *ortho* LNOF #2. A small but freestanding reflection at $Q = 1.85$ Å^{-1} is assigned to this phase as can be seen in Fig. S2d, e and 3a–c. Since oxygen release is detected during its formation and decay it is assumed to be even more oxygen deficient than mono LNOF. As this intermediate phase has been observed by Wissel *et al.*[27] on electrochemical fluorination of $La_2NiO_3F_2$, it is in agreement with our supposed overall anion content between that of $La_2NiO_3F_2$ and mono LNOF. The weight fraction of this phase is at its maximum between 240–400 minutes of reaction time, which is also well-reflected in the heatmap plot (Fig. 3b). Afterwards, the weight fraction decreases to zero towards the end of the reaction.

As described above, *ortho* LNOF #2 disappears gradually under formation of the final fourth phase $La_2NiO_3F_2$ *Cccm*, reflecting the high stability of nickel in its divalent oxidation state. In both reactions, due to the increased oxygen partial pressure above the sample, Ag_2O starts to form from Ag which is the decomposition product of AgF. However, as the oxygen is flushed out by the N_2 flow, the weight fraction of Ag_2O also decreases again, and Ag is observed as the only reaction product left after extended heating at 300 °C.

The release of oxygen upon the chemical fluorination of La_2NiO_4 and the formation of $La_2NiO_3F_2$ as a final product are a clear indicator that all intermediate phases are not stable at the final temperature of 300 °C and decompose under oxygen release. However, the onset of oxygen release in the fluorination of La_2NiO_4 occurs only after reaching 300 °C, contrary to La_2CoO_4 which already releases oxygen at 250 °C. Performing this fluorination reaction at a lower temperature (210 °C and 250 °C) did not result in a phase pure product either. At 210 °C, a mixture of the starting compound, *ortho* LNOF #1 and mono LNOF were formed, and after heating to 250 °C the decomposition into *ortho* LNOF #2 and $La_2NiO_3F_2$ started very slowly (see Fig. S4). No oxygen or fluorine could be detected in the mass spectrometer which is most likely due to very slow decomposition and formation of Ag_2O which did not decompose at the applied temperatures. It has to be noted that phases observed on AgF-based fluorination also clearly differ from what is observed applying a non-oxidative chemical fluorination with PVDF.[26]

The lattice parameters of all RP-phases during the fluorination process are displayed in Fig. 4a and b for La_2CoO_4 and La_2NiO_4 respectively.

For La_2CoO_4 the observed trend is comparably simple. The starting oxide La_2CoO_4 shows an increase in the *c*-lattice parameter while the fluorination is taking place, indicating a partial insertion of fluorine into the lattice[23] beyond a small potential contribution from thermal expansion considering the reported thermal expansion behavior of RP-type materials.[28,29] In the *a*–*b*-plane the lattice parameters do not change

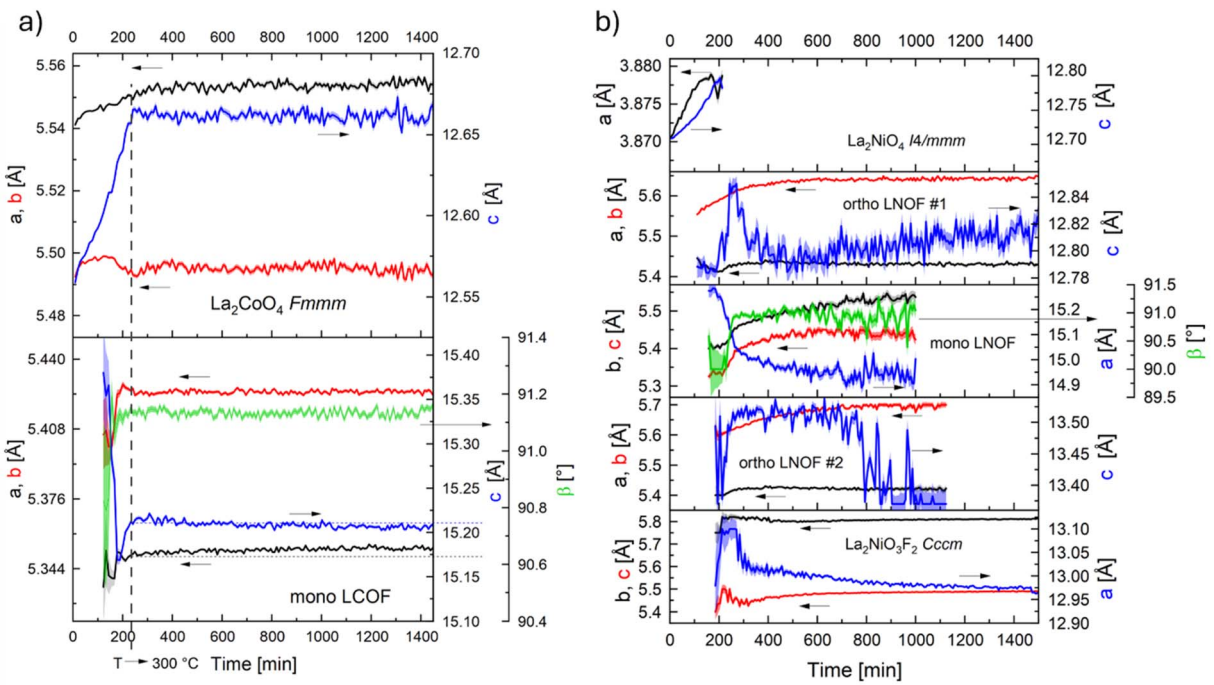

Fig. 4 Lattice parameters of all RP-phases present during the fluorination of (a) La_2CoO_4 and (b) La_2NiO_4 during with AgF from VTXRD. The dashed lines in the bottom graph of (a) indicate the values for *b* and *c* as 300 °C was reached to make the slight change better visible. The numerical error bars for all values have been combined into confidence intervals which are indicated by a shaded region around the respective graphs. The values of the lattice parameters are not displayed if the weight fraction is smaller than 3 wt%.

drastically. For mono LCOF we observe stronger changes. Here the *c*-axis decreases parallel to the increase in weight fraction, followed by an additional small decrease during the 300 °C temperature hold. The *a*-lattice parameter on the other hand shows only a very small expansion (even after reaching the maximum temperature of 300 °C), which could indicate an increased space requirement in the octahedral plane due to reduction of the cobalt ions in the fluorinated phase. In contrast, the drop in the *c*-lattice parameter indicates a removal from ions on interstitial or apical octahedral sites. This is in-line with the oxygen release observed in the same timeframe showing that mono LCOF shows a flexibility towards the oxygen content, releasing oxygen as the temperature is increased which is reflected in the change of lattice parameters. We acknowledge that due to the small lattice parameter changes, the oxygen release is most likely also small.

Due to complex phase evolution behavior of the fluorination of La_2NiO_4 using AgF, the lattice parameters of all phases are affected by larger scattering and error, but general trends can still be derived. The *a*- and *c*-lattice parameters of the initial La_2NiO_4 *I*4/*mmm* phase are mostly affected by thermal expansion and become expectedly unreliable as the weight fraction drops to zero, which is why they are only shown up to ~200 min. For *ortho* LNOF #1, the *b*- and *c*-lattice parameters significantly increase only during the heating stage. Therefore, we assume this to be resulting from thermal expansion. During the 300 °C temperature hold, the *b*-lattice parameter expands minutely while the other lattice parameters are constant.

The *a*-lattice parameter of mono LNOF in the space group *C*2/*c* (please note that the standard setting of this space group has *a* as longest axis) drops from an initial value of 15.3 Å to around 14.9 Å while a monoclinic distortion builds up and the corresponding angle increases significantly to ~91° as the *c*-lattice parameter drops. The initial state is very similar to what was reported for orthorhombic $La_2NiO_4F_{1.8}$ by Nowroozi *et al.*,[25] while the final state is closer to the $La_2NiO_3F_3$ phase with monoclinic symmetry reported by Wissel *et al.*[27] Further, an increase of the lattice parameters in the equatorial plane is in-line with this comparison as Nowroozi *et al.* determined smaller equatorial lattice parameters for $La_2NiO_4F_{1.8}$ than Wissel *et al.* reported for $La_2NiO_3F_3$ ($a \sim 5.36$ Å, $b \sim 5.31$ Å *vs.* $b \sim 5.47$ Å, $c \sim 5.38$ Å). These similarities in the lattice parameters further support the above statement that mono LNOF transitions from orthorhombic to monoclinic symmetry while releasing oxygen from the lattice.

We observed that the *a*-lattice parameter (long axis) of *ortho* LNOF #2 is decreasing by ~0.2 Å after a very brief initial increase while the equatorial plane is expanding in both directions by ~0.1 Å simultaneously. These trends are like what we observed for mono LNOF and indicate that the oxygen detected by the mass spectrometer also originates from *ortho* LNOF #2. All lattice parameters of $La_2NiO_3F_2$ *Cccm* reflect the same trend as was observed for mono LNOF and *ortho* LNOF #2, decreasing of the long axis while the equatorial plane expands. The values at the end of the experiment are close to what was observed by Wissel *et al.* for $La_2NiO_3F_2$,[22] even though the *a*-axis is slightly expanded which might be due to the higher temperature of the *in situ* measurement.

In summary, the fluorination of La_2CoO_4 leads to the formation of a single fluorinated phase (mono LCOF) accompanied by oxygen release. The lattice parameters of mono LCOF indicate minor release of oxygen also after phase formation. On the other hand, La_2NiO_4 shows a cascade of different phases: La_2NiO_4 *I*4/*mmm* → *ortho* LNOF #1 → mono LNOF → *ortho* LNOF #2 → $La_2NiO_3F_2$ *Cccm*. The last three phases all show lattice parameter changes indicative of oxygen release, which is reflected by the mass spectrometer signals as the total time of oxygen being detected extends to ~500–600 minutes compared to only ~250 minutes for La_2CoO_4

3.2 Differential electrochemical mass spectrometry

We conducted DEMS on La_2CoO_4 and La_2NiO_4 during electrochemical fluorination at 140 °C and 163 °C. This electrochemical fluorination represents a reaction equation of

$$La_2MO_4 + xF^- \rightarrow La_2MO_{4-y}F_x + xe^- + \frac{y}{2}O_2 \quad (2)$$

for which the amount of *y* needs to be determined. The temperature of 163 °C was chosen since it best reflects the operation temperature of FIBs from previous publications[23,25,30] (see Fig. S5). Fig. 5 shows the DEMS data for the electrochemical fluorination of composites containing La_2CoO_4 and La_2NiO_4 as well as without active material (only 90 wt% $La_{0.9}Ba_{0.1}F_{2.9}$ and 10 wt% Super P) at 163 °C including charging curve, and gas evolution values obtained by integration of the ion current converted to ppm values. The DEMS data for electrochemical fluorination at 140 °C can be seen in Fig. S6, with similar trends and further reduced overall gas release. The gases observed and their appearance is complex and thus requires detailed discussion with reference to what is known on other battery materials, *e.g.* in the lithium-ion battery field.

CO_2 release is a known phenomenon in lithium-ion batteries and lithium solid-state batteries which is attributed to surface carbonate residues which can either decompose chemically or electrochemically.[31–33] TG-MS measurements of the components of our cathode composite revealed that all components contain carbonate residues which however only decompose at temperatures >250 °C (see Fig. S8), thus ruling out a direct thermal release at the applied DEMS temperatures (see also Fig. S7).

The only reasonable assumption for the origin of NO is the release of NO_x from the decomposition of nitrates. As NO_2 is a very unstable molecule and electron ionization tends to generate mostly NO molecules and O atoms, the absence of a signal for NO_2 is well explained.[34] The origin of nitrate decomposition is attributed to the $La_{0.9}Ba_{0.1}F_{2.9}$ solid electrolyte *via* TG-MS since it shows significant mass loss accompanied by NO release when heated to 550 °C (see Fig. S8). We conclude that the precursors for the solid electrolyte contain small amounts of nitrate impurities which could not be removed by any of the pretreatment steps as described above.

No signal at $m/z = 32$ which would represent O_2 could be detected in the fluorination of any pellet. However, CO and CO_2 can also be formed as byproducts of evolved oxygen reacting

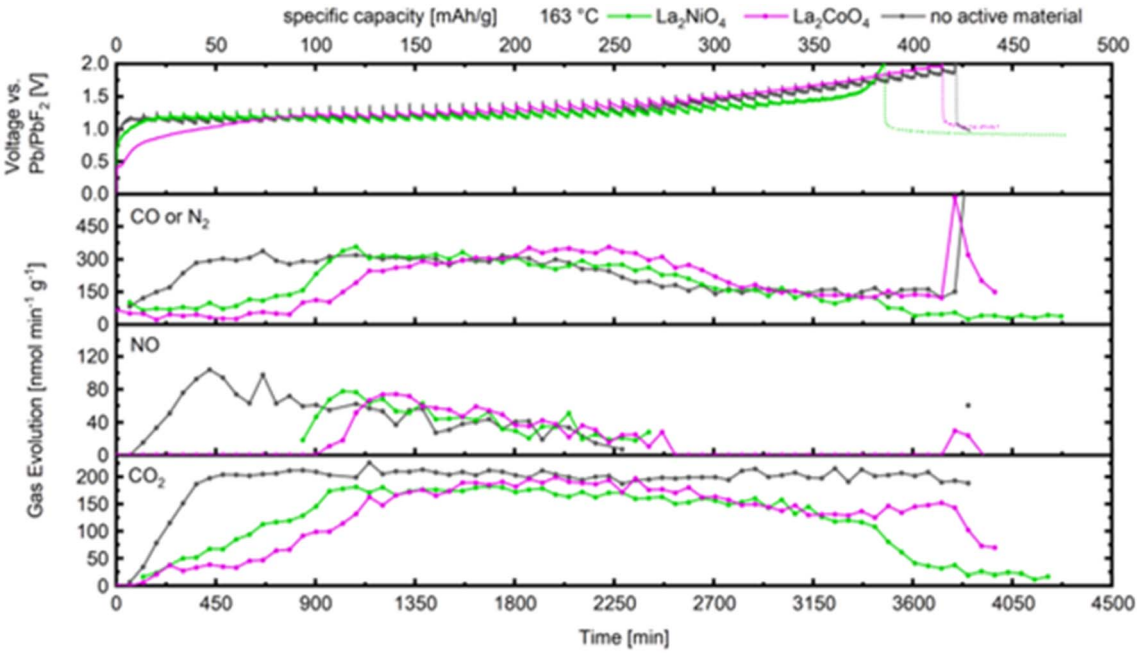

Fig. 5 DEMS measurement of La_2CoO_4, La_2NiO_4 and a composite without active material in electrochemical fluorination at 163 °C. Dotted lines in the potential graph indicate that the charging has stopped and the cell is now in relaxation. The mass spectrometer was calibrated for CO_2 by measuring air (420 ppm of CO_2). The values for CO/N_2 and NO are to be considered semi-quantitative. The capacity for the cell without active material is calculated for the same mass of active material used in the cells containing either La_2CoO_4 or La_2NiO_4. Since the mass of carbon is the same in all these cells, this way of depicting the capacity best reflects the contribution of carbon to the capacity and gas evolution for the cells containing active materials.

with carbon-containing components in the cell setup.[13] To test if this could contribute to the observed CO and CO_2, a mixture of $KMnO_4$ and La_2CoO_4 (as a catalyst to lower the decomposition temperature) was heated to 163 °C to intentionally release O_2 in the DEMS setup. While CO and CO_2 could be observed when the decomposition started, a signal for $m/z = 32$ was always present alongside (see Fig. S9), showing that if O_2 is formed in the DEMS setup, it can also be detected directly.

A composite without active material was measured in order to reflect the gas evolution upon carbon fluorination, and shows large amounts of gas evolution in the DEMS measurement at 163 °C. Gas evolution sets in directly when charging begins and increases rapidly until the evolution of CO (note that the value for CO can be affected by outgassing of adsorbed nitrogen) and CO_2 reaches stable values after ~40 mAh g^{-1}. NO evolution peaks at this capacity and slowly decreases afterwards. While the evolution of CO_2 remains very constant until the charging process is completed, CO evolution decreases slightly after reaching a capacity of ~250 mAh g^{-1}. Since both the solid electrolyte and the carbon additive were shown to contain impurities which release CO_2 in a TG-MS measurement (see Fig. S8), CO_2 release observed in the cells with active material is explained from this behavior. Since CO cannot originate from carbonate decomposition, other contaminations and functional groups in the carbon additive (Super P) used must lead to CO release. The potential during carbon fluorination (as was reported to take place in ASS-FIBs[24,27,30,35]) shows a plateau around 1.2–1.3 V *vs.* Pb/PbF_2 at 163 °C or closer to 1.4 V *vs.* Pb/PbF_2 at 140 °C and shows a characteristic sawtooth-like shape. The sharp increase in potential always correlates exactly with the moment when the cell container is flushed, *i.e.* the atmosphere is exchanged for a pure argon atmosphere and all evolved gases are flushed out, indicating a sensitivity of the carbon composite to some gaseous species.

For the composite containing La_2CoO_4, the charging potential shows a plateau around 0.7–1.0 V *vs.* Pb/PbF_2 when charged at 163 °C, which is not affected by sawtooth-like features. Nevertheless, release of CO and CO_2 in the order of 30–40 nmol min^{-1} g^{-1} and 25 nmol min^{-1} g^{-1} respectively can be detected already. After reaching ~70–80 mAh g^{-1}, the potential increases to around 1.2–1.3 V *vs.* Pb/PbF_2, very close to the potential of the cell without active material, and the sawtooth-like features start to appear. At the same time, CO_2 evolution starts to increase linearly, while CO evolution only starts increasing at ~120 mAh g^{-1}, peaking around 175 nmol min^{-1} g^{-1} and 350 nmol min^{-1} g^{-1} for CO_2 and CO respectively between 200–250 mAh g^{-1}. This maximum in gas evolution closely matches the rate observed for the cell without active material; in combination with the absence of a signal of O_2, we conclude that the oxygen contained within CO_2 and CO thus must nearly exclusively originate from the decomposition of the carbon additive. Therefore, we assume that ~120 mAh g^{-1} marks the end of fluorination of La_2CoO_4 and further capacity and gas release is originating from the solid electrolyte and carbon additive. Since the theoretical capacity of La_2CoO_4 for the intercalation of two fluoride ions per formula unit is 133

mAh g^{-1} and no O_2 release is indicated, we describe the electrochemically fluorinated product as $La_2CoO_4F_{2-d}$, implying nearly full occupation of the interstitial sites but refraining from stating a more precise fluoride content.

At 140 °C, the charging plateau of La_2CoO_4 is observed at a higher potential of ~1.3 V *vs.* Pb/PbF_2, which is still below what is observed for the cell without active material. Evolution of the $m/z = 28$ signal is heavily affected by outgassing of surface-adsorbed N_2 at the beginning (compare Fig. S7), but as N_2 is disappearing the value is stable around 75 nmol min^{-1} g^{-1}, which again is attributed to CO. CO_2 evolution starts out at 25 nmol min^{-1} g^{-1} but slowly increases in a roughly linear fashion. After reaching 100 mAh g^{-1}, CO evolution rapidly increases to 300 nmol min^{-1} g^{-1}, while the sawtooth shape in the charging curve reaches its largest extent. The evolution of CO_2 which was steadily increasing now peaks at 150 nmol min^{-1} g^{-1}. As the voltage increases to 2 V *vs.* Pb/PbF_2, the evolution of CO and CO_2 decreases again. The general trend of the gas evolution values at 140 °C is similar to the fluorination at 163 °C, only showing an increase in the gas evolution rates slightly earlier, which is in-line with reduced carbon fluorination as judged by the difference in capacity in cell without active material.

For La_2NiO_4, the CO evolution behavior at 163 °C is very similar to La_2CoO_4, only that the peak evolution of ~300 nmol min^{-1} g^{-1} is already reached at ~110 mAh g^{-1} and the fluorination potential is higher at ~1.2–1.3 V *vs.* Pb/PbF_2, very close to the potential of the cell without active material, indicating that the fluorination of La_2NiO_4 is strongly overlaid by this side reaction. Judging from the capacity where gas evolution peaked, the absence of O_2 signals as well as the fact that the amount of the CO/CO_2 formed is well explained from the side reaction of the carbon additive, we describe the electrochemically fluorinated product as $La_2NiO_4F_{2-d}$ with similar reasoning as for $La_2CoO_4F_{2-d}$ (the specific capacity of $La_2NiO_4F_2$ is also 133 mAh g^{-1}). When charging at 140 °C, the behavior of La_2NiO_4 is different, showing a charging plateau at ~1.4 V *vs.* Pb/PbF_2 which is also very close to that of cell without active material. During the whole charging process, CO evolution is rather constant at 70–100 nmol min^{-1} g^{-1}, while CO_2 evolution is very similar to that of La_2CoO_4, increasing from 0 to 75 nmol min^{-1} g^{-1}. The CO evolution is even smaller than what was observed for cell without active material, while the CO_2 evolution is only slightly smaller. Again, no evolution of NO could be observed.

The diffraction patterns of the La_2CoO_4 and La_2NiO_4 cells after the DEMS measurement (see Fig. S12a for La_2CoO_4 at 163 °C, Fig S13a for La_2NiO_4 at 163 °C and Fig. S10a and b for both materials at 140 °C) show that the La_2CoO_4 has fully been converted to $La_2CoO_4F_{2-d}$ while for La_2NiO_4, a small weight fraction of *ortho* LNOF #1 as also observed in chemical fluorination is present alongside $La_2NiO_4F_{2-d}$. Again, this is in agreement with the absence of oxygen evolution in the DEMS measurements, in accordance with an unchanged oxygen content of the pristine and charged cathode materials. The La_2NiO_4 cell charged at 140 °C (Fig. S10a) shows only a minor weight fraction of $La_2NiO_4F_{2-d}$ while two phases of *ortho* LNOF #1 are present, indicative of an incomplete fluorination of the active material. Since the potential was very similar to the cell without active material, we assume that significant carbon fluorination took place, which was not the case for the La_2CoO_4 cell at 140 °C which charged at a lower potential, obtaining full conversion to $La_2CoO_4F_{2-d}$ (Fig. S10c).

In summary, the DEMS measurements of La_2CoO_4 and La_2NiO_4 in electrochemical fluorination show that significant amounts of CO_2 and CO are released from contaminations in the solid electrolyte and carbon additives. When an active material is employed in the cell, those gas releases are postponed to higher states of charge, and an evolution of O_2 is not indicated, *i.e.* all oxygen released and contained within CO/CO_2 can be explained from the decomposition of the carbon additive. This shows that the evolution of gases from La_2CoO_4 and La_2NiO_4 in electrochemical fluorination is not accompanied by major oxygen release, contrary to what was observed in chemical fluorination as discussed in Section 3.1. Most likely, the lower temperature used in the DEMS measurements as compared to fluorination with AgF stabilizes higher oxidation states, therefore inhibiting oxygen-release.

3.3 Thermal stability of electrochemically fluorinated La_2CoO_4 and La_2NiO_4

Since the chemical fluorination experiments have shown that high oxygen contents of fluorinated materials are unstable at elevated temperatures, we also investigated the thermal stability of the charged state of the cathode materials La_2CoO_4 and La_2NiO_4. For this, the pellets fluorinated in the DEMS measurements were heated to 300 °C in dynamic vacuum while recording XRD patterns continuously, completing a scan every 30 minutes. The resulting heatmap-plots of the XRD patterns are shown in Fig. 6a for La_2CoO_4 and Fig. 6b La_2NiO_4, while the weight fractions obtained from Rietveld-refinement are displayed in Fig. 6c and d respectively.

We observe that electrochemically obtained $La_2CoO_4F_{2-d}$ decomposes about 60 minutes after 300 °C is reached, and a new phase starts to appear which could be refined by adopting the structure of $La_2NiO_3F_2$ for Co instead of Ni changing the lattice parameters only minimally (see Fig. S11, S12e and f). We observed that this material $La_2CoO_3F_2$ was also obtained in defluorination experiments of $La_2CoO_3F_3$ and a full description will be published along with the structural characterization $La_2CoO_3F_3$ in a separate article. Prior to the decomposition reaction, the lattice parameters of $La_2CoO_4F_{2-d}$ (Fig S11a) show a characteristic expansion of the equatorial plane accompanied by a contraction of the long axis, which was previously linked to oxygen release from the lattice. Obtaining a phase of the stoichiometry $La_2CoO_3F_2$ is in-line with the implied oxygen loss from $La_2CoO_4F_{2-d}$ even though we did not detect it directly, as this VTXRD-setup is not equipped with a mass spectrometer.

The electrochemically obtained $La_2NiO_4F_{2-d}$ decomposes almost completely within 30 minutes after a temperature of 300 °C is reached, resulting in a mixture of *ortho* LNOF #2 and $La_2NiO_3F_2$ as observed in chemical fluorination and an increased amount of *ortho* LNOF #1 compared to the start of the

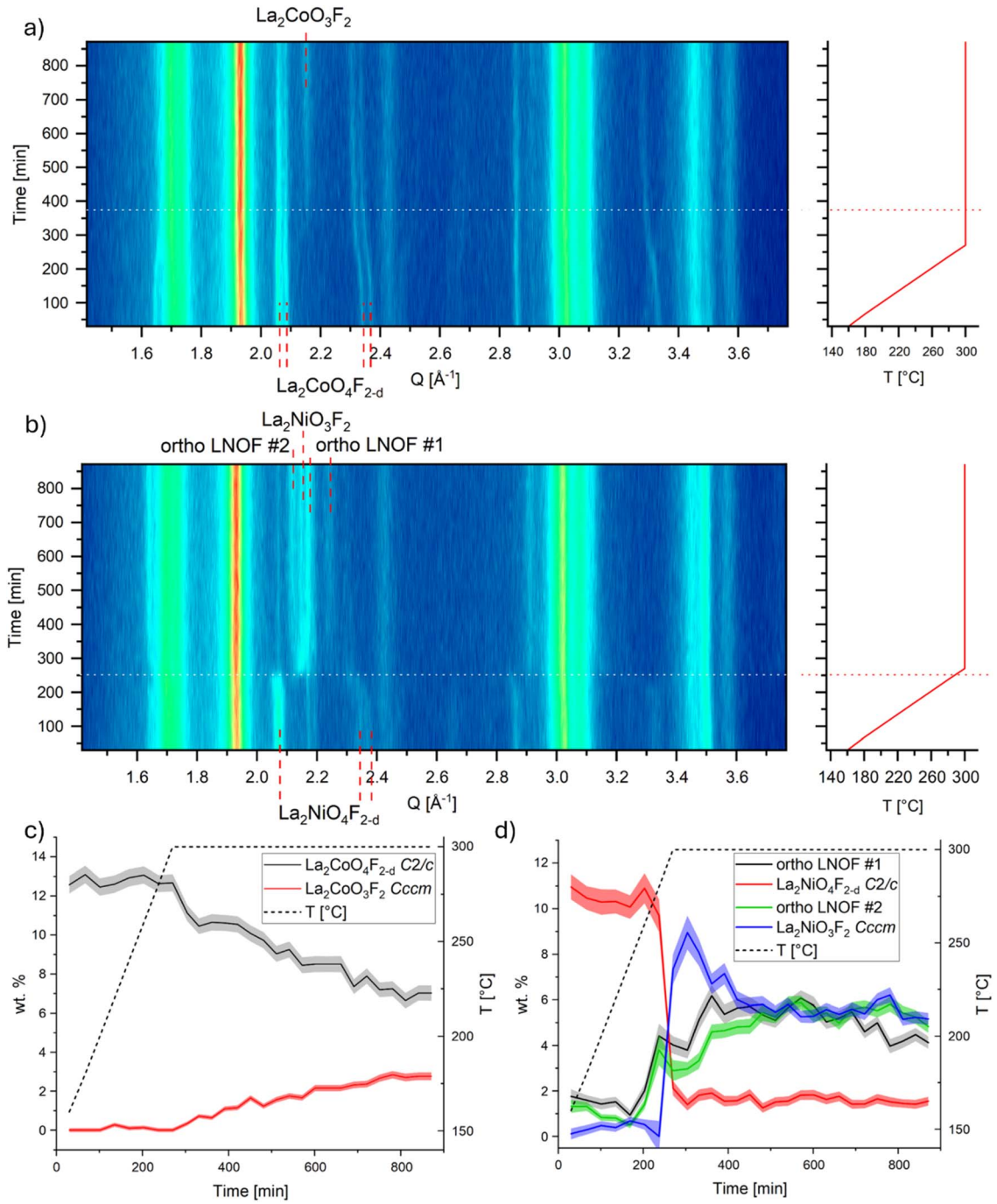

Fig. 6 Heatmap-plot of the VTXRD patterns of electrochemically fluorinated (a) La_2CoO_4 and (b) La_2NiO_4 pellets. The weight fractions obtained by Rietveld-refinement area shown in (c) for La_2CoO_4 and (d) for La_2NiO_4. The dotted red/white line marks the time and temperature where the decomposition products appear.

decomposition reaction (see Fig. S13). This implies that LNOF #1 is not only an intermediate of the fluorination of La_2NiO_4 to $La_2NiO_4F_{2-d}$ but also a decomposition product. Also, the lattice parameters of $La_2NiO_4F_{2-d}$ and $La_2NiO_3F_2$ (Fig. S11b) show very similar trends to the lattice parameters observed in chemical fluorination. As mentioned before, this characteristic expansion of the equatorial plane, contraction of the long axis and increase of the monoclinic angle implies oxygen release from both structures. The more rapid decomposition of $La_2NiO_4F_{2-d}$ in comparison to $La_2CoO_4F_{2-d}$ might be related to the different strength of overlap of the Ni/Co-d and O-2p energy levels. For lithium-ion batteries, it is known that the larger overlap of the Ni-d and O-2p orbitals tends to facilitate oxygen release through hole formation in the O-2p orbitals.[36,37] Similar trends in thermal stability could also be observed for $LiNi_xMn_yCo_zO_2$ cathode materials where higher nickel content correlated with lower decomposition temperature and more rapid decomposition reactions[38]

We conclude that electrochemically obtained $La_2CoO_4F_{2-d}$ is of a different anion composition than mono LCOF obtained from chemical fluorination. While the latter is stable towards decomposition at 300 °C, only showing minor lattice parameter changes, the prior decomposes under formation of an oxygen deficient monoclinic phase and $La_2CoO_3F_2$. This supports the results from DEMS, showing that electrochemical fluorination does not lead to oxygen release as was detected in chemical fluorination. On the contrary, electrochemically obtained $La_2NiO_4F_{2-d}$ and its chemically fluorinated counterpart mono LNOF, both decompose at 300 °C showing similar trends in lattice parameters and the same decomposition products. Since the DEMS measurements also show no oxygen evolution, and oxygen was only detected in the chemical fluorination when mono LNOF transitioned from orthorhombic to monoclinic symmetry, we assume the electrochemically obtained $La_2NiO_4F_{2-d}$ and chemically obtained mono LNOF to be of very similar anion composition.

4 Conclusions and outlook

In this study, we report the oxidative fluorination pathways of La_2CoO_4 and La_2NiO_4 using AgF which are accompanied by oxygen release as detected by *in situ* variable-temperature X-ray diffraction with coupled mass spectrometry. Further, we report the evolution of CO, CO_2 and NO for all-solid-state fluoride ion batteries using La_2NiO_4 or La_2CoO_4 as cathode active materials additive using a novel setup for differential electrochemical mass spectrometry which allows for measurements at elevated temperatures up to 200 °C. Oxygen release from the cathode materials could not be detected, highlighting electrochemical fluorination as a synthesis method for low-temperature fluorination to obtain compounds which are unstable at higher temperatures. Insights gained from X-ray diffraction during thermal decomposition of the charged cathode composites show that the charged cathode materials are thermally stable up to 220 °C, showing significant lattice parameter changes above 220 °C and decomposing at 300 °C.

The findings reported here further provide a completely new perspective on the mechanisms discussed for topochemical fluorination reactions[39–42] in dependence of the reaction temperature and oxidation strength of the fluorination agent used: since the electrochemical fluorination at lower temperatures can reduce the Fermi Level while at the same time kinetically blocking the oxygen release, we highlight the potential of the electrochemical approach for making new materials beyond battery application with novel electronic and/or magnetic properties. Thus, the complex interaction of charge transition levels in perovskite-related materials, their temperature-dependent accessibility and the relation to the electronic structure of the materials facilitates a novel important approach for choosing the most promising synthesis strategy for a targeted oxyfluoride compound.[43]

As shown in an earlier publication,[24] La_2NiO_4 and La_2CoO_4 are able to provide high cyclic stability with excellent coulombic efficiency after initial side reactions decreased within the first few cycles. At this point, we can state that gas release from contaminations in the cathode composite in early cycles is a possible origin for the low initial coulombic efficiency, which would mark gas release from the composite as an activation process, not a degradation mechanism.

Further research could try to purify the solid electrolyte and conductive carbon to avoid gas evolution from the composites. Also, more careful attempts to obtain orthorhombic $La_2NiO_4F_{2-d}$ phase pure would enable an in-depth characterization of this compound not possible before.

Author contributions

T. A.: conceptualization, data curation, formal analysis, investigation, methodology, software,[44,45] visualization, writing – original draft; J. J.: data curation, investigation, methodology, validation, visualization, writing – review & editing; F. F.: data curation; D. S.: methodology, resources; O. C.: funding acquisition, investigation, project administration, supervision, validation, writing – review & editing.

Conflicts of interest

There are no conflicts of interest to declare.

Data availability

The data supporting this article have been included as part of the supplementary information (SI). Supplementary information is available. See DOI: **https://doi.org/10.1039/d5ta07033c**.

The code for automated Rietveld refinements as well as integration of mass spectrometry data can be found at **https://github.com/TommiAalto-IMW/batchXRD** **https://github.com/TommiAalto-IMW/DEMSIntegration** with DOI: **https://doi.org/10.5281/zenodo.16993766** **https://doi.org/10.5281/zenodo.16993870** The version of the code employed for this study is version 1.0 and 1.2 respectively.

Acknowledgements

We thank Rotraut Merkle from the Max-Planck-Institute for Solid-State Research for letting us use the mass spectrometer and all the kind assistance with its operation. Special thanks to Florian Kaiser for the constant support in the construction and testing of the DEMS setup. Further thanks to the Institute of Chemical Process Engineering at the University of Stuttgart for access to their mass spectrometer in the earlier stages of the development of the DEMS setup. OC acknowledges funding *via* the collaborative research center FLAIR (Fermi level engineering applied to oxide electroceramics), which is supported by the German Research Foundation (DFG) (Project-ID No. 463184206, SFB 1548).

References

1 T.-Y. Huang, *et al.*, Deconvolution of intermixed redox processes in Ni-based cation-disordered Li-excess cathodes, *Energy Environ. Sci.*, 2021, **14**(3), 1553–1562.

2 M. M. Rahman and F. Lin, Oxygen Redox Chemistry in Rechargeable Li-Ion and Na-Ion Batteries, *Matter*, 2021, **4**(2), 490–527.
3 R. A. House, *et al.*, The role of O_2 in O-redox cathodes for Li-ion batteries, *Nat. Energy*, 2021, **6**(8), 781–789.
4 N. Guerrini, *et al.*, Charging Mechanism of Li_2MnO_3, *Chem. Mater.*, 2020, **32**(9), 3733–3740.
5 M. Farahmandjou, *et al.*, Oxygen redox chemistry in lithium-rich cathode materials for Li-ion batteries: Understanding from atomic structure to nano-engineering, *Nano Mater. Sci.*, 2022, **4**(4), 322–338.
6 Z. Yin, *et al.*, Approaching a stable oxygen redox reaction in lithium-rich cathode materials: structural perspectives from mechanism to optimization, *J. Mater. Chem. A*, 2022, **10**(37), 19387–19411.
7 Q. Li, *et al.*, Improving the oxygen redox reversibility of Li-rich battery cathode materials via Coulombic repulsive interactions strategy, *Nat. Commun.*, 2022, **13**(1), 1123.
8 S. Sharifi-Asl, *et al.*, Oxygen Release Degradation in Li-Ion Battery Cathode Materials: Mechanisms and Mitigating Approaches, *Adv. Energy Mater.*, 2019, **9**(22), 1900551.
9 S. Kobayashi, *et al.*, Atomic-Scale Observations of Oxygen Release Degradation in Sulfide-Based All-Solid-State Batteries with Layered Oxide Cathodes, *ACS Appl. Mater. Interfaces*, 2022, **14**(34), 39459–39466.
10 R. Jung, *et al.*, Oxygen Release and Its Effect on the Cycling Stability of $LiNi_xMn_yCo_zO_2$ (NMC) Cathode Materials for Li-Ion Batteries, *J. Electrochem. Soc.*, 2017, **164**(7), A1361.
11 J. K. Papp, *et al.*, A comparison of high voltage outgassing of $LiCoO_2$, $LiNiO_2$, and Li_2MnO_3 layered Li-ion cathode materials, *Electrochim. Acta*, 2021, **368**, 137505.
12 R. Jung, *et al.*, Temperature Dependence of Oxygen Release from $LiNi_{0.6}Mn_{0.2}Co_{0.2}O_2$ (NMC622) Cathode Materials for Li-Ion Batteries, *J. Electrochem. Soc.*, 2018, **165**(11), A2869.
13 F. Strauss, *et al.*, Gas Evolution in Lithium-Ion Batteries: Solid versus Liquid Electrolyte, *ACS Appl. Mater. Interfaces*, 2020, **12**(18), 20462–20468.
14 T. Bartsch, *et al.*, Gas Evolution in All-Solid-State Battery Cells, *ACS Energy Lett.*, 2018, **3**(10), 2539–2543.
15 R. Jung, *et al.*, Oxygen Release and Its Effect on the Cycling Stability of $LiNi_xMn_yCo_zO_2$ (NMC) Cathode Materials for Li-Ion Batteries, *J. Electrochem. Soc.*, 2017, **164**, A1361.
16 D. Zhang, *et al.*, Cathode Design Based on Nitrogen Redox and Linear Coordination of Cu Center for All-Solid-State Fluoride-Ion Batteries, *J. Am. Chem. Soc.*, 2025, **147**(7), 5649–5657.
17 Y. Wang, *et al.*, Oxyfluoride Cathode for All-Solid-State Fluoride-Ion Batteries with Small Volume Change Using Three-Dimensional Diffusion Paths, *Chem. Mater.*, 2022, **34**(23), 10631–10638.
18 H. Miki, *et al.*, Double-Layered Perovskite Oxyfluoride Cathodes with High Capacity Involving O–O Bond Formation for Fluoride-Ion Batteries, *J. Am. Chem. Soc.*, 2024, **146**(6), 3844–3853.
19 Z. Cao, *et al.*, Revealing the Unusual Mechanism of Mixed Cationic and Anionic Redox in Oxyfluorosulfide Cathode for All-Solid-State Fluoride-Ion Batteries, *Chem. Mater.*, 2024, **36**(4), 1928–1940.
20 Y. Wang, *et al.*, Ultra-High-Capacity of Earth-Abundant Cathodes Enabled by Excess Fluoride-Ion Insertion/Extraction, *Adv. Energy Mater.*, 2025, 2406131.
21 R. Zhang, M. S. Senn and M. A. Hayward, Directed Lifting of Inversion Symmetry in Ruddlesden–Popper Oxide–Fluorides: Toward Ferroelectric and Multiferroic Behavior, *Chem. Mater.*, 2016, **28**(22), 8399–8406.
22 K. Wissel, *et al.*, Topochemical Fluorination of La_2NiO_{4+d}: Unprecedented Ordering of Oxide and Fluoride Ions in $La_2NiO_3F_2$, *Inorg. Chem.*, 2018, **57**(11), 6549–6560.
23 M. A. Nowroozi, *et al.*, La_2CoO_4: a new intercalation based cathode material for fluoride ion batteries with improved cycling stability, *J. Mater. Chem. A*, 2018, **6**(11), 4658–4669.
24 T. H. Aalto, *et al.*, Toward Carbon-Free Cathodes for Fluoride Ion Batteries: Deconvoluting Effects of Active Material and Conductive Additive on Charging and Cyclic Stability, *Batteries Supercaps*, 2025, 2500195.
25 M. A. Nowroozi, *et al.*, High cycle life all-solid-state fluoride ion battery with La_2NiO_{4+d} high voltage cathode, *Commun. Mater.*, 2020, **1**(1), 27.
26 J. Jacobs, *et al.*, Unveiling the Fluorination Pathway of Ruddlesden–Popper Oxyfluorides: A Comprehensive In Situ X-ray and Neutron Diffraction Study, *J. Am. Chem. Soc.*, 2025, **147**(11), 9739–9751.
27 K. Wissel, *et al.*, Electrochemical Reduction and Oxidation of Ruddlesden–Popper-Type $La_2NiO_3F_2$ within Fluoride-Ion Batteries, *Chem. Mater.*, 2021, **33**(2), 499–512.
28 Y. Hu, *et al.*, $La_{2-x}Sr_xCoO_{4-\delta}$ ($x = 0.9, 1.0, 1.1$) Ruddlesden-Popper-type layered cobaltites as cathode materials for IT-SOFC application, *Int. J. Hydrogen Energy*, 2013, **38**(7), 3064–3072.
29 L. V. Makhnach, V. V. Pankov and P. Strobel, High-temperature oxygen non-stoichiometry, conductivity and structure in strontium-rich nickelates $La_{2-x}Sr_xNiO_{4-\delta}$ (x=1 and 1.4), *Mater. Chem. Phys.*, 2008, **111**(1), 125–130.
30 M. A. Nowroozi, *et al.*, $LaSrMnO_4$: Reversible Electrochemical Intercalation of Fluoride Ions in the Context of Fluoride Ion Batteries, *Chem. Mater.*, 2017, **29**(8), 3441–3453.
31 T.-Y. Huang, *et al.*, Chemical Origin of in Situ Carbon Dioxide Outgassing from a Cation-Disordered Rock Salt Cathode, *Chem. Mater.*, 2024, **36**(13), 6535–6546.
32 S. E. Renfrew, L. A. Kaufman and B. D. McCloskey, Altering Surface Contaminants and Defects Influences the First-Cycle Outgassing and Irreversible Transformations of $LiNi_{0.6}Mn_{0.2}Co_{0.2}O_2$, *ACS Appl. Mater. Interfaces*, 2019, **11**(38), 34913–34921.
33 S. E. Renfrew and B. D. McCloskey, Residual Lithium Carbonate Predominantly Accounts for First Cycle CO_2 and CO Outgassing of Li-Stoichiometric and Li-Rich Layered Transition-Metal Oxides, *J. Am. Chem. Soc.*, 2017, **139**(49), 17853–17860.
34 P. J. Linstrom and W. G. Mallard, The NIST Chemistry WebBook: A Chemical Data Resource on the Internet, *J. Chem. Eng. Data*, 2001, **46**(5), 1059–1063.

35 Y. Matsuo, *et al.*, Charge-discharge behavior of fluorine-intercalated graphite for the positive electrode of fluoride ion shuttle battery, *Electrochem. Commun.*, 2020, **110**, 106626.
36 A. Manthiram and T. Muraliganth, Lithium Intercalation Cathode Materials for Lithium-Ion Batteries, in *Handbook of Battery Materials*, 2011, pp. 341–375.
37 M. Dixit, *et al.*, Origin of Structural Degradation During Cycling and Low Thermal Stability of Ni-Rich Layered Transition Metal-Based Electrode Materials, *J. Phys. Chem. C*, 2017, **121**(41), 22628–22636.
38 S.-M. Bak, *et al.*, Structural Changes and Thermal Stability of Charged LiNixMnyCozO2 Cathode Materials Studied by Combined In Situ Time-Resolved XRD and Mass Spectroscopy, *ACS Appl. Mater. Interfaces*, 2014, **6**(24), 22594–22601.
39 E. E. McCabe and C. Greaves, Fluorine insertion reactions into pre-formed metal oxides, *J. Fluorine Chem.*, 2007, **128**(4), 448–458.
40 C. Greaves and M. G. Francesconi, Fluorine insertion in inorganic materials, *Curr. Opin. Solid State Mater. Sci.*, 1998, **3**(2), 132–136.
41 H. Kageyama, *et al.*, Exploring Structures and Properties through Anion Chemistry, *Bull. Chem. Soc. Jpn.*, 2019, **92**(8), 1349–1357.
42 Y. Kobayashi, Y. Tsujimoto and H. Kageyama, Property Engineering in Perovskites via Modification of Anion Chemistry, *Annu. Rev. Mater. Res.*, 2018, **48**, 303–326.
43 A. Klein, *et al.*, The Fermi energy as common parameter to describe charge compensation mechanisms: A path to Fermi level engineering of oxide electroceramics, *J. Electroceram.*, 2023, **51**(3), 147–177.
44 Aalto, *T. DEMSIntegration. GitHub*, DOI: **10.5281/zenodo.16993870**.
45 Aalto, *T. batchXRD. GitHub*, DOI: **10.5281/zenodo.16993766**.